

Research Article

Open Access



Axial chlorine-induced asymmetric cobalt single-atom coordination fields for boosting oxygen reduction reaction

Xi-Rong Jiang¹, Guo-Dong Xie¹, Jun-Hao Li¹, Wen-Jie Huang¹, Jun-Da Lu¹, Pan Xie¹, Yan Dong¹, Wen-Da Ma¹, Yi-Da Deng^{1,2}, Xue-Rong Zheng^{1,2}

¹State Key Laboratory of Marine Resource Utilization in South China Sea, School of Materials Science and Engineering, Hainan University, Haikou 570228, Hainan, China.

²School of Materials Science and Engineering, Key Laboratory of Advanced Ceramics and Machining Technology of Ministry of Education, Tianjin University, Tianjin 300072, China.

Correspondence to: Prof. Wen-Jie Huang, Prof. Xue-Rong Zheng, and Jun-Da Lu, State Key Laboratory of Marine Resource Utilization in South China Sea, School of Materials Science and Engineering, Hainan University, No. 58 Renmin Avenue, Haikou 570228, Hainan, China. E-mail: wj_huang@hainanu.edu.cn; xrzh@hainanu.edu.cn; lujundaacc@163.com

How to cite this article: Jiang, X. R.; Xie, G. D.; Li, J. H.; Huang, W. J.; Lu, J. D.; Xie, P.; Dong, Y.; Ma, W. D.; Deng, Y. D.; Zheng, X. R. Axial chlorine-induced asymmetric cobalt single-atom coordination fields for boosting oxygen reduction reaction. *Microstructures* 2025, 5, 2025077. <https://dx.doi.org/10.20517/microstructures.2024.189>

Received: 29 Dec 2024 **First Decision:** 7 Apr 2025 **Revised:** 10 Apr 2025 **Accepted:** 22 Apr 2025 **Published:** 2 Jul 2025

Academic Editors: Dingsheng Wang, Nana Wang **Copy Editor:** Xing-Yue Zhang **Production Editor:** Xing-Yue Zhang

Abstract

The development of oxygen reduction reaction (ORR) catalysts with high activity, stability, and economic applicability plays a decisive role in reducing expenses and enhancing the discharge performance of seawater-based zinc-air batteries (SWZABs). Co- and Fe-based single-atom catalysts (M-N₄-C) with metal-N₄ structure offer advantages of well-defined active structure and high active site utilizations. However, the oxygen electrocatalytic performance of M-N₄-C remains a formidable challenge due to the highly stable centrosymmetric electronic structure. To overcome the dilemma, we develop a Co-N₄Cl-C with axial coordination of Cl atoms. The axial coordination drags the Co atoms out of the Co-N₄ centrosymmetric configuration. This alters the electronic configuration of Co single-atom sites, resulting in a valence state change from +1.83 to +0.67 and forming a localized negative charge environment. These alternations enhance the electronic orbital overlap between Co single-atom sites and oxygen species, promote the rapid evolution of *OOH intermediates, and inhibit the adsorption of toxic Cl⁻ ions, ensuring the ORR kinetics and stability. Co-N₄Cl-C exhibits a high oxygen reduction onset potential of 1.05 mV and a half-wave potential of 0.88 mV vs. the reversible hydrogen electrode. The SWZAB, featuring a Co-N₄Cl-C catalyst cathode, Zn anode, and NaCl electrolyte supplemented with KOH, reaches a discharge voltage platform of 1.27 V and a peak power density of 179 mW·cm⁻², even at 10 a current density



© The Author(s) 2025. **Open Access** This article is licensed under a Creative Commons Attribution 4.0 International License (<https://creativecommons.org/licenses/by/4.0/>), which permits unrestricted use, sharing, adaptation, distribution and reproduction in any medium or format, for any purpose, even commercially, as long as you give appropriate credit to the original author(s) and the source, provide a link to the Creative Commons license, and indicate if changes were made.



of $\text{mA}\cdot\text{cm}^{-2}$. This study sheds important light on advancing single-atom catalysts with superior ORR performance and economic viability.

Keywords: Co-N₄-C single-atom catalyst, chlorine axial coordination, electronic structure, oxygen reduction kinetics, seawater-based zinc-air battery

INTRODUCTION

The seawater-based zinc-air batteries (SWZABs) exhibit prominent advantages, including low cost, intrinsic safety, and high theoretical energy density^[1]. For SWZABs, the oxygen reduction reaction (ORR) constitutes a pivotal electrochemical process^[2-4]. The catalytic activity of the cathode significantly dominates key performance indicators of these systems, such as rate capacity, energy density, and operational lifespan^[5]. The ORR is characterized by a complex four-electron transfer mechanism that involves multiple steps of proton-coupled electron transfer, which results in slow kinetic rates^[6]. The fundamental challenge is that the electronic configuration of the metal sites in the catalytic active centers remains suboptimal, leading to excessively strong or weak adsorption/desorption of the oxygen-species intermediates. Additionally, the suboptimal electronic structure fails to effectively impede the adsorption of Cl⁻ ions in chloride-rich seawater electrolytes, resulting in the poisoning and corrosion of metal active sites and consequently diminishing the operational lifespan^[7]. Therefore, the regulation of electronic structure in metal sites is essential for enhancing ORR activity and stability.

Currently, commercial noble metal catalysts (e.g., Pt, Pd) feature an excellent intrinsic electronic structure, demonstrating impressive ORR activity^[8]. However, the widespread implementation of these catalysts is restricted by the scarcity of resource distribution and high costs^[9]. Moreover, the Co- and Fe-based non-noble metal catalysts with suboptimal electronic structures exhibit strong binding energy with oxygen-containing intermediates, resulting in sluggish kinetic behavior^[10-12]. For Co- and Fe-based compounds, including oxides, nitrides, and phosphides, systematic regulation of their electronic structures has been attempted through various strategies, such as doping, vacancies, and strain. However, the performance improvement from these strategies remains limited, which fails to fundamentally address the issue of low intrinsic activity^[13-16].

Single-atom catalytic materials with metal-nitrogen (M-N₄, M = Co, Fe, etc.) structures present several advantageous characteristics of homogeneous distribution of catalysts, including the uniformity of active sites and the adjustable interactions with ligands, while integrating the significant stability and recyclability of heterogeneous catalysts^[17]. Notably, the uniformity of active sites ensures a high proportion of exposed atoms, high active site utilizations, and well-defined active sites at the single-atom level, thereby offering the potential to surpass bulk materials^[18]. However, these catalysts typically adopt the M-N₄ configuration with a centrosymmetric structure, which tends to exhibit a highly stable electronic structure^[19-21]. The stable electronic structure increases the 3d-band electron density of the transition metal single atom, thereby reducing its orbital interaction with O 2p electrons and imposing a higher thermodynamic energy barrier for the generation of the *OOH intermediate^[22,23]. Although extensive efforts have been devoted to adjusting the first and second coordination shells, these strategies have demonstrated limited efficacy in altering the centrosymmetric configuration of the M-N₄ site^[24-27]. The activity of these single-atom catalysts is urgently in need of enhancement^[28]. Moreover, the electronic structure of M-N₄ configuration with a centrosymmetric structure is insufficient to hinder the adsorption of Cl⁻ ions on Co single-atom sites, which leads to the poisoning of the Co single-atom sites, thereby reducing its stability^[29]. Therefore, there is an urgent need to optimize the M-N₄ electronic structure of metal single-atom catalysts to achieve both rapid kinetics and

strong resistance to Cl^- ion poisoning.

In this work, we axially coupled electron-rich and highly electronegative Cl atoms to the Co-N_4 coordination structure without altering its tetracoordination, thereby designing the $\text{Co-N}_4\text{Cl-C}$ catalyst. The $\text{Co-N}_4\text{Cl}$ coordination structure consists of a Cl atom coordinated to the Co-N_4 structure in an adjacent 2-dimensional (2D) carbon layer. The axial coordination of Cl atoms reconstructs the local electronic environment and optimizes the electronic configuration of the Co single-atom sites, thereby significantly enhancing the intrinsic ORR activity. This axial coordination of Cl transfers electrons to Co single-atom sites, reducing the electron density at the Co site in $\text{Co-N}_4\text{Cl-C}$ from +1.83 to +0.67. The reduction in electron density enhances the orbital coupling between Co single-atom sites and oxygen species, facilitating the generation of $^*\text{OOH}$ intermediates and thus accelerating the ORR kinetics. This ensures an efficient four-electron transfer mechanism. Meanwhile, the axial coordination of Cl atoms forms a localized negative charge environment, reducing the adsorption of Cl^- ions from the reaction medium, mitigating the poisoning of cobalt single-atom sites and thus improving stability. Compared to pristine $\text{Co-N}_4\text{-C}$, the oxygen reduction onset potential (E_{onset}) and half-wave potential ($E_{1/2}$) of $\text{Co-N}_4\text{Cl-C}$ catalyst are enhanced by 0.16 and 0.08 V, respectively, achieving values of 1.05 and 0.88 V vs. reversible hydrogen electrode (RHE). The $E_{1/2}$ of $\text{Co-N}_4\text{Cl-C}$ surpasses that of $\text{Co}_3\text{O}_4/\text{G}$ (0.74 V), FeNiP-NPHC (0.83 V), Pt/C-Ir/C (0.85 V), D-FeCo@NHC (0.85 V), and $\text{Fe}_x\text{N-NC}$ (0.87 V)^[30-33]. Moreover, we designed the SWZAB, which consists of a $\text{Co-N}_4\text{Cl-C}$ cathode, Zn anode, and 0.5 M NaCl electrolyte with 6 M KOH. This SWZAB achieves a maximum energy density of $179 \text{ mW}\cdot\text{cm}^{-2}$ and a specific capacity of $778 \text{ mAh}\cdot\text{g}^{-1}$, while maintaining a stable discharge voltage plateau of 1.27 V even under a high current density of $10 \text{ mA}\cdot\text{cm}^{-2}$.

EXPERIMENTAL DETAILS

Materials

Cobalt acetylacetonate [$\text{Co}(\text{acac})_3$, 98%], zinc nitrate hexahydrate [$\text{Zn}(\text{NO}_3)_2\cdot 6\text{H}_2\text{O}$, 98%], methanol (CH_3OH , 99.8%), and Pt/C catalyst were sourced from Shanghai Aladdin Biochemical Technology Co., Ltd. 2-methylimidazole (2-mlm, 98%), NaCl (99.5%), and KOH (95.0%) were supplied by from Shanghai Macklin Biochemical Co., Ltd. A 5 wt.% Nafion solution, prepared in a mixture of lower aliphatic alcohols and deionized water, was supplied by Shanghai Yien Chemical Technology Co., Ltd. All experimental agents were utilized without undergoing additional purifying processes.

Fabrication of the Co-ZIF-8 precursor

A 2.60 g quantity of 2-mlm was solubilized in 35 mL of CH_3OH , followed by continuous agitation for 30 min, culminating in the formation of Solution I. Concurrently, 1.20 g of $\text{Zn}(\text{NO}_3)_2\cdot 6\text{H}_2\text{O}$ and 0.36 g of $\text{Co}(\text{acac})_3$ were homogeneously dispersed in 15 mL of CH_3OH and subjected to vigorous stirring for 30 min, yielding Solution II. Subsequently, Solution I was amalgamated with Solution II and underwent continuous agitation for an extended period of 24 h. The mixed solution was filtered and washed six times with CH_3OH . The resulting Co-ZIF-8 powder was dehydrated at 60°C for an extended period in a vacuum drying oven.

Fabrication of the Co-N₄-C catalyst

The Co-ZIF-8 precursor underwent pyrolysis at $1,000^\circ\text{C}$ for a duration of 2 h under an argon gas atmosphere, with a thermal ramp rate of 5°C per minute, and was then permitted to cool to ambient temperature in a natural manner. The resultant black powder was termed as the $\text{Co-N}_4\text{-C}$ catalyst.

Synthesis of the Co-N₄Cl-C catalyst

The Co-ZIF-8 precursor was combined with NaCl powder in a mass proportion of 4:1 and subjected to grinding for 1 h. Subsequently, the mixture was subjected to pyrolysis under a flow of Ar gas at $1,000^\circ\text{C}$ for

a duration of 2 h, with a thermal ramp rate of 5 °C per minute. The resultant black powders were washed with deionized water, separated via centrifugation, and ultimately dried at 60 °C in a vacuum oven for 12 h. The obtained black powders were designated as the Co-N₄Cl-C catalyst.

Synthesis of the nitrogen-doped carbon catalyst

A 2.60 g quantity of 2-mlm was solubilized in 35 mL of CH₃OH to yield Solution I. Next, 1.20 g of Zn(NO₃)₂·6H₂O was dispersed in 15 mL of CH₃OH to form Solution III, which was then added to Solution I, followed by uninterrupted agitation for 24 h. The resultant white precipitate was isolated via vacuum filtration, washed three times with CH₃OH, and dried overnight at 60 °C in a vacuum oven. Finally, the white precipitate was subjected to pyrolysis at 1,000 °C in an argon condition for 2 h, with a temperature increase rate of 5 °C per minute. The acquired product was referred to as the nitrogen-doped carbon (NC) catalyst.

Characterizations

The X-ray diffraction (XRD, Rigaku, SmartLab XRD) utilizing Cu-K α radiation was performed to examine the phase constitution. The morphological and microstructural properties were characterized by scanning electron microscope (SEM, Thermo Scientific, Verios G4 UC), transmission electron microscopy (TEM, Thermo Scientific, Talos F200X G2) equipped with energy dispersive spectroscopy (EDS), and high-angle annular dark-field scanning TEM (HAADF-STEM, JEOL, JEM-ARM200F). The quantitative analysis of the Co element content was accomplished through inductively coupled plasma OES spectrometer (ICP-OES, SPECTRO Analytical, SPECTRO-blue). The chemical environment of Co and Cl atoms was scrutinized by X-ray photoelectron spectroscopy measurements (XPS, VG Scientific ESCALAB250). The electronic configuration and coordination structure of Co atom-single sites were probed by X-ray absorption spectroscopy (XAS, easyXAFS, easyXAFS300+). Standard Co foil and CoO powder were deployed as references for Co⁰ and Co²⁺ chemical states, respectively. The Co-Pc and CoCl₂ were utilized as references for the Co-N and Co-Cl coordination structures, respectively. The obtained extended X-ray absorption fine structure (EXAFS) data were treated in accordance with the standard systemic procedures using the ATHENA module applied in the IFEFFIT software package.

Electrochemical tests

To fabricate the slurry, 10 mg of the catalyst were incorporated into a mixture comprising 80 μ L of Nafion (5 wt.%) and 920 μ L of isopropanol alcohol, followed by ultrasonication for 1 h. The electrochemical behavior of the ORR was appraised utilizing a conventional three-electrode setup. 4 μ L of the paste was applied to a polished glassy carbon electrode, yielding a catalyst loading weight of 0.2 mg·cm⁻², which was employed as the working electrode. A Pt foil with an area of 1 cm × 1 cm was engaged as the counter electrode. A Hg/HgO electrode, impregnated with a 1 M KOH solution, was leveraged as the reference electrode. A mixture of 0.5 M NaCl and 1 M KOH was deployed as the electrolyte. All reported potentials were referenced to the RHE using the following expression: $E_{vs. RHE} = E_{vs. Hg/HgO} + 0.098 V + 0.059 \times pH$. The rotating disk electrode (RDE) was interfaced with an electrochemical workstation (Ivium) and a controlled speed rotator (AFMSRCE, Pine Instruments). The ORR polarization curves were captured at a scan rate of 5 mV·s⁻¹ in the electrolyte under O₂- and N₂-saturated conditions. The ORR linear sweep voltammetry (LSV) curves on RDE were documented over disk rotation speeds spanning from 400 to 2,500 rpm. The ORR stability measurement was conducted at ambient temperature in the O₂-saturated electrolyte containing 0.5 M NaCl and 1 M KOH.

Calculation of electron transfer numbers

Electron transfer numbers (n) were determined using the Koutecky-Levich Equations (1) and (2)^[34]:

$$\frac{1}{J} = \frac{1}{J_L} + \frac{1}{J_K} = \frac{1}{B\omega^{1/2}} + \frac{1}{J_K} \quad (1)$$

$$B = 0.62nFC_0D_0^{2/3}V^{-1/6} \quad (2)$$

where J indicates the measured response current density, J_k and J_L refer to the kinetic and limiting current densities, ω denotes the angular velocity of the disk, F signifies the Faraday constant ($96,500 \text{ C}\cdot\text{mol}^{-1}$), n represents the electron transfer numbers throughout ORR process, C_0 reflects the bulk concentration of O_2 in KOH ($1.2 \times 10^{-6} \text{ mol}\cdot\text{cm}^{-3}$), D_0 means the diffusion coefficient in KOH ($1.9 \times 10^{-5} \text{ cm}^2\cdot\text{s}^{-1}$), and V refers to the kinematic viscosity in the electrolyte (0.1 M KOH: $0.01 \text{ cm}^2\cdot\text{s}^{-1}$)^[35].

Calculation of mass activity and turnover frequency

The value of mass activity ($\text{A g}_{\text{metal}}^{-1}$) was computed by the following Equation (3)^[36]:

$$\text{Mass activity} = \frac{J_K \times A \times 10^{-3}}{M_{\text{metal}}} \quad (3)$$

where J_k and A represent the kinetic current density ($\text{mA}\cdot\text{cm}^{-2}$) and the geometric electrode area (cm^2), and M_{metal} signifies the loading mass of active centers in the electrocatalyst. The Co single-atom sites were regarded as active centers, and their content was validated by ICP-OES testing.

The value of turnover frequency (TOF) was inferred through the Equation (4)^[36]:

$$\text{TOF} = \frac{J_K \times A \times N_e \times 10^{-3}}{4 \times M_{\text{metal}} \times N_A / M} \quad (4)$$

where N_e refers to the electron number per Coulomb (6.24×10^{18}), N_A signifies Avogadro's constant (6.02×10^{23}), and M represents the molar mass of Co atom ($58.93 \text{ g}\cdot\text{mol}^{-1}$).

Fabrication of SWZABs

A solution composed of 6 M KOH and 0.5 M NaCl functioned as a simulated alkaline seawater electrolyte. This electrolyte was maintained in an O_2 -saturated state over prolonged durations to assess the electrochemical performance of SWZABs. A zinc plate featuring an active area of $1 \text{ cm} \times 1 \text{ cm}$ was utilized as the anode. The catalyst was applied to carbon paper to form the air membrane electrode for the cathode, with the catalyst-coated area measuring $1 \text{ cm} \times 1 \text{ cm}$.

RESULTS AND DISCUSSION

The preparation procedure for the Co- N_4Cl -C catalyst is schematized in Figure 1. Initially, $\text{Co}(\text{acac})_3$ and $\text{Zn}(\text{NO}_3)_2$ interact with 2-mlm to form the Co-ZIF-8 organic ligand. Subsequently, Cl atoms are incorporated into the Co- N_4 coordination structure through a molten NaCl-assisted strategy, after which Co- N_4Cl -C is obtained. For comparison, the synthesis process for the Co- N_4 -C catalyst is identical to that of Co- N_4Cl -C, except for the exclusion of NaCl.

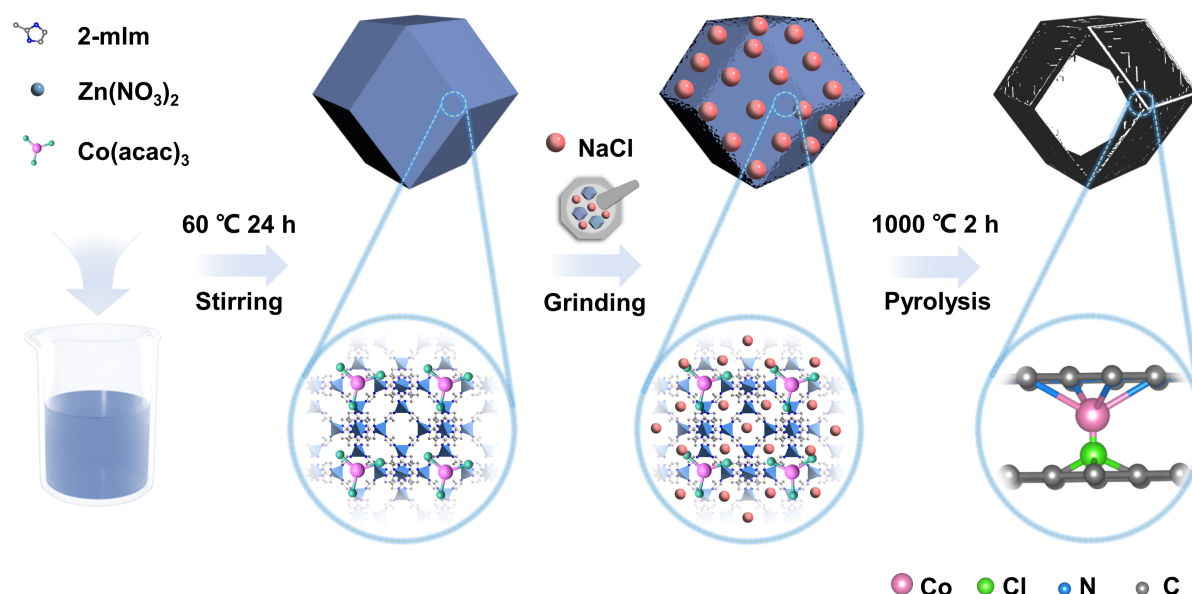


Figure 1. Visual representation of the synthetic procedures for the Co-N₄Cl-C catalyst. 2-mlm: 2-methylimidazole.

The morphological characteristics of Co-N₄-C and Co-N₄Cl-C were first examined using SEM and TEM. The Co-N₄-C catalyst exhibits a solid dodecahedral morphology, with particles observed to be approximately 80 nm after pyrolysis [Figure 2A and B], which is similar to the Co-ZIF-8 precursor [Supplementary Figure 1]. In contrast, with the molten NaCl-assisted strategy, the dodecahedral structure of Co-N₄Cl-C undergoes slight collapse, shrinking to a size of 50 nm [Figure 2C and D]. Meanwhile, the dodecahedral configuration evolves from a solid structure into a porous hollow carbon skeleton [Figure 2D]. The formation of the porous hollow carbon framework is attributed to the high polarity of NaCl, which melts and infiltrates the Co-ZIF-8 dodecahedral structure during pyrolysis^[37-39]. This process induces localized etching between adjacent C and Cl atoms, generating pores and facilitating the introduction of Cl atoms. EDS mapping was employed to verify the spatial distribution of multiple elements within the catalyst. The comparison of EDS mapping results [Figure 2E and F] ascertains that C, N, Co, and additional Cl elements are evenly dispersed throughout the Co-N₄Cl-C, while C atoms are enriched in edge regions. Based on the fitting curves of the EDS spectrum, the content of Cl atoms in the Co-N₄Cl-C catalyst was determined to be 0.17 wt.% [Supplementary Figure 2]. The Cl content is significantly lower than the nominal concentration, showing that most Cl atoms are volatilized during 1,000 °C pyrolysis, leaving only trace residues. To clarify the specific localization of Co atoms on the carbon substrate, the HAADF-STEM test was conducted. The isolated bright spots attest to the monatomic distribution of Co atoms in Co-N₄-C [Figure 2G] and Co-N₄Cl-C [Figure 2H]. Moreover, no well-defined lattice fringes are observed. Accordingly, the selected area electron diffraction (SAED) patterns [Figure 2G and H, inset] reveal concentric rings of diffuse scattering, indicating the amorphous structure of Co-N₄-C and Co-N₄Cl-C^[40]. The XRD patterns of Co-N₄-C and Co-N₄Cl-C [Supplementary Figure 3] exhibit a broad peak instead of sharp diffraction peaks within the range of 15° to 35°, indicating the non-crystalline nature. To elucidate the degree of atomic order in the microstructures of these catalysts, Raman spectroscopy was implemented [Supplementary Figure 4]. The distinguishing peaks at 1,350 and 1,580 cm⁻¹ can be matched to the D and G bands, respectively. For the Co-N₄-C and Co-N₄Cl-C catalysts, the high I_G/I_D ratio of 1.08 suggests a disordered carbon network. The XRD and XPS analyses jointly corroborate the amorphous structure of these catalysts^[41]. In ICP-MS analysis [Supplementary Table 1], the Co single-atom contents in Co-N₄-C and Co-N₄Cl-C are confirmed to be 1.27 and 1.44 wt.%, respectively, indicating that the introduction of Cl has

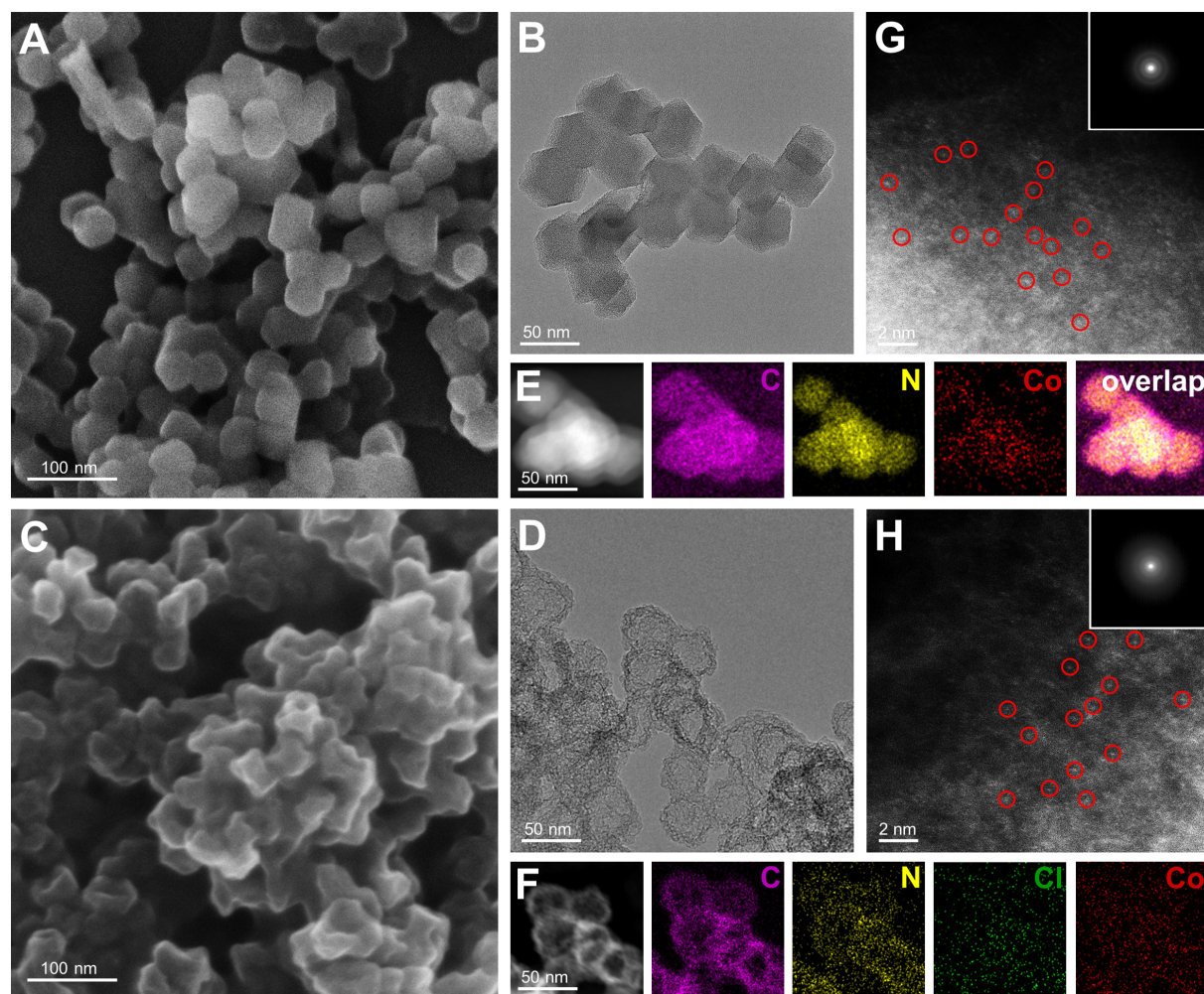


Figure 2. (A and C) The SEM pictures; (B and D) TEM pictures; (E and F) corresponding EDS mappings; and (G and H) HAADF-STEM images of Co-N₄-C and Co-N₄Cl-C, respectively. SEM: Scanning electron microscope; TEM: transmission electron microscopy; EDS: energy dispersive spectroscopy; HAADF-STEM: high-angle annular dark-field scanning TEM.

no adverse effect on the loading amount of Co single-atom sites.

The XPS detection technology was performed to reveal the surface chemical environment of catalysts. In the high-resolution Cl 2*p* spectra [Figure 3A], the prominent characteristic peak is observed at 197 eV for Co-N₄Cl-C^[42]. For the high-resolution Co 2*p* spectra [Supplementary Figure 5] of Co-N₄-C and Co-N₄Cl-C catalysts, peaks are observed at 778.8 and 793.6 eV, which are characteristics of the Co⁰ 2*p*_{3/2} and Co⁰ 2*p*_{1/2} orbitals, respectively. Prominent peaks at 780.7 and 795.6 eV are indicative of the oxidation status of the Co²⁺ 2*p*_{3/2} and Co²⁺ 2*p*_{1/2} orbitals, respectively. Moreover, satellite peaks are identified at 785.3 and 800.2 eV^[43]. For comparison, the intensity of the Co⁰ peaks in Co-N₄Cl-C is markedly higher than that in Co-N₄-C, signifying a diminished oxidation state of Co atoms. Through the integration and fitting of the peak intensities associated with Co⁰ and Co²⁺, the chemical states of Co atoms were ascertained to be +0.68 and +1.72 for the Co-N₄Cl-C and Co-N₄-C catalysts, respectively. To further confirm the modulation of the local electronic configuration and coordination characteristic in the Co single-atom sites by Cl atoms, the XAS measurement was performed in transmission mode. The Co K-edge X-ray absorption near-edge structure (XANES) spectra for Co-N₄-C and Co-N₄Cl-C catalysts are positioned between the reference

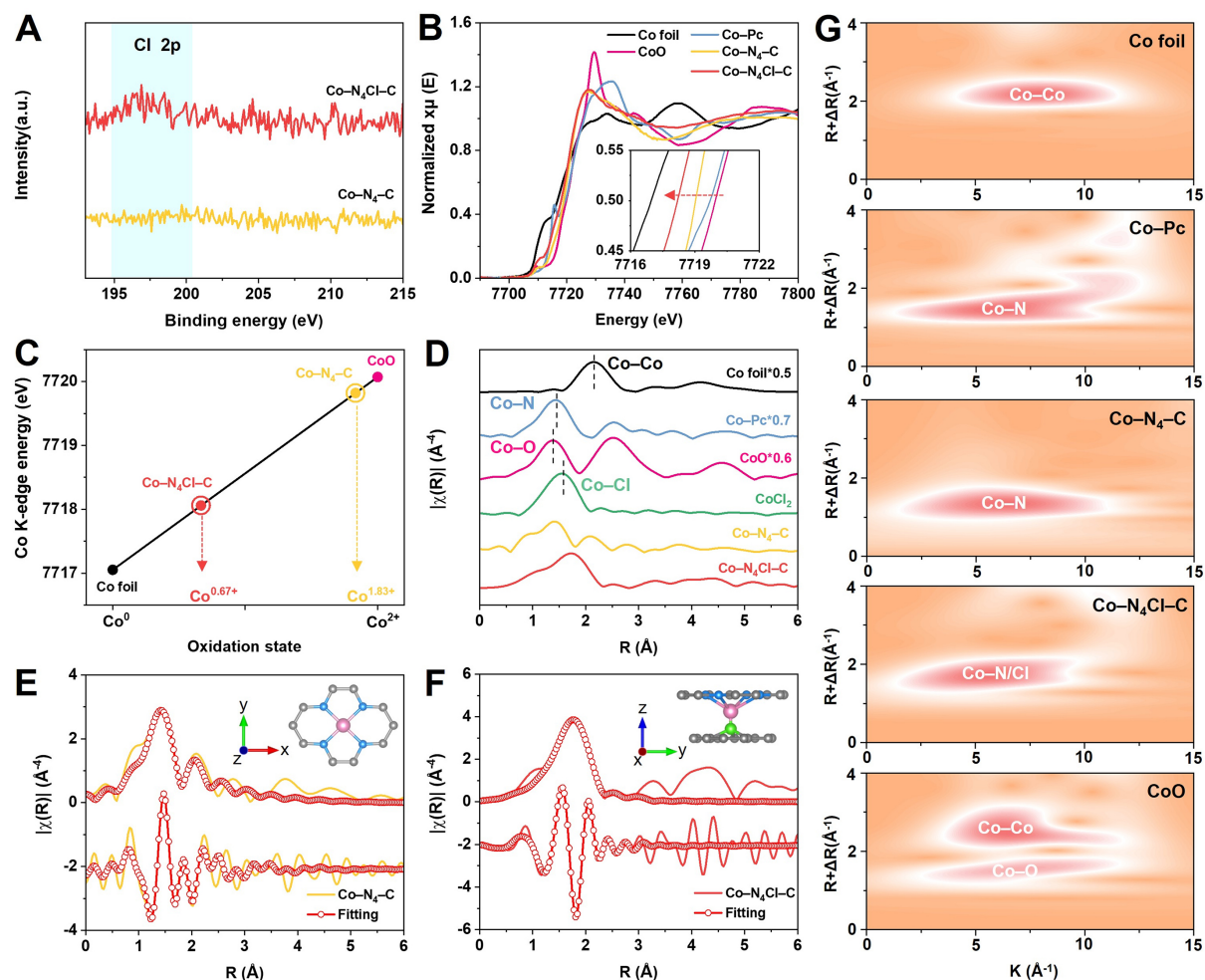


Figure 3. (A) Cl 2p XPS spectra of Co-N₄-C and Co-N₄Cl-C; (B) Co-K-edge XANES spectra of samples and references (the inset shows the magnified pre-edge XANES region); (C) The determined Co K-edge positions and oxidation statuses of Co in the Co-N₄Cl-C and Co-N₄-C; (D) FT of the EXAFS spectra of samples and references. First-shell fitting of FT of EXAFS spectra for (E) Co-N₄-C and (F) Co-N₄Cl-C. EXAFS spectra were fitted using the FEFF 6.0 code (the insets show the structure of the Co-N₄-C and Co-N₄Cl-C; the balls in gray, blue, pink, and green correspond to C, N, Co, and Cl atoms, respectively); (G) WT of samples and references. XPS: X-ray photoelectron spectroscopy; XANES: X-ray absorption near-edge structure; EXAFS: extended X-ray absorption fine structure; FT: Fourier transform; FEFF: full multiple scattering; WT: wavelet-transformed.

spectra of Co foil and CoO, implying that the oxidation state of Co atoms in the catalysts falls between the range 0 and +2 [Figure 3B]. According to the nearly linear portion of the elevating Co K-edge (7,716–7,712 eV) of samples and references for integration and defining the integrated average intensity as the K-edge position, a linear relationship can be obtained and used to identify the oxidation state of Co atoms in the catalysts [Figure 3B, inset]. The Co K-edge positions of Co foil and CoO are located at 7,717.05 and 7,720.07 eV, respectively. Based on the Co K-edge position in the Co-N₄-C catalyst (7,719.82 eV), its valence state is determined to be +1.83 [Figure 3C]. After the coordination of Cl atoms in the Co-N₄Cl-C catalyst, the Co K-edge position shifts from 7,719.82 to 7,718.06 eV, corresponding to a reduction in the oxidation state of Co atoms from +1.83 to +0.67. These calculated oxidation statuses of Co atoms are in agreement with the XPS results.

The K^3 -weighted EXAFS spectra were derived from the Fourier-transformed (FT) original XAS data. In the first shell of the R -space between 1 and 2 Å, the characteristic peak of Co-N₄-C emerges at 1.4 Å, similar to that in Co-Pc, corresponding to the Co-N₄ coordination structure [Figure 3D]^[44]. By contrast, this characteristic peak for Co-N₄Cl-C shifts to 1.7 Å, resulting in a change in the first-shell coordination environment of Co metal sites. Moreover, in the Co-N₄-C and Co-N₄Cl-C catalysts, neither the characteristic peaks associated with Co-Co and Co-O scattering paths are detected in the second shell of the R -space spectra within the range of 2 to 2.5 Å, indicating that the metal coordination structure consists solely of Co single-atom sites^[45,46]. To further elucidate the coordination number and bond length of Co single-atom sites, the EXAFS curves were quantitatively analyzed using fitting routines [Figure 3E and F]. Compared with Co-N₄-C, in the first coordination shell, the Co-N coordination number of Co-N₄Cl-C catalyst evolves from 4.1 to 3.6, and the Co-Cl coordination number is calculated to be 0.9 [Supplementary Table 2]^[22,47]. Notably, the generation of the Co-Cl coordination structure stretches the Co-N bond length to 1.7 Å, bringing both to a comparable scale. Additional insights into the atomic arrangement of Co are provided by the EXAFS oscillation curves in k -space [Supplementary Figure 6] and wavelet-transformed (WT) Co K-edge EXAFS contour plots [Figure 3G]. The intensity maxima of the Co-N₄-C and Co-N₄Cl-C catalysts appear at 6.5 and 6.2 Å⁻¹, corresponding to Co-N and Co-N/Cl scattering paths, respectively, consistent with the structural analysis of R -space. Based on these XAS results, the structure of Co-N₄Cl-C involves the formation of an axial coordination structure between individual Cl atoms and Co single-atom site in the adjacent 2D carbon layer, pulling the Co atom away from the planar centrosymmetric Co-N₄ environment [Figure 3F, inset]. This pulling process induces a tip effect, which triggers the accumulation of local negative charges and results in partial electron transfer from the chlorine atoms to the cobalt single-atom sites, thereby reducing the valence state of the cobalt single-atom sites^[48,49].

To evaluate the benefit of Cl atomic axial coordination, the ORR performances of Co-N₄Cl-C, Co-N₄-C, NC, and commercial Pt/C catalysts were systematically examined in 1 M KOH and 0.5 M NaCl electrolyte. The conventional three-electrode setup was employed for electrochemical measurements. This setup includes the catalyst as the working electrode, a Pt foil as the counter electrode, and an Hg/HgO electrode (saturated with 1 M KOH) as the reference electrode. In the linear sweep voltammetry (LSV) analysis conducted on the RDE at a scan rate of 5 mV·s⁻¹ under a spinning rate of 1,600 rpm in N₂-saturated and O₂-saturated conditions, over a potential span of 0.2 to 1.2 V vs. RHE, the current densities of the Co-N₄-C, Co-N₄Cl-C, Pt/C, and NC catalysts show a notable increase under O₂-saturated condition relative to those under N₂-saturated condition [Figure 4A and Supplementary Figure 7], demonstrating the occurrence of ORR process rather than other electrochemical reactions (such as double-layer capacitance, ion intercalation, and hydrogen evolution). After background calibration using the current densities of LSV curves under N₂-saturated conditions, the Co-N₄Cl-C catalyst delivers oxygen reduction E_{onset} and $E_{1/2}$ of 1.05 and 0.88 V vs. RHE, outperforming the Co-N₄-C (0.89 and 0.8 V), Pt/C (0.94 and 0.85 V), and NC (0.76 and 0.71 V). Meanwhile, the $E_{1/2}$ of Co-N₄Cl-C is higher than that of most reported catalysts in seawater-based systems, such as Co₃O₄/G (0.74 V), FeNiP-NPHC (0.83 V), Pt/C-Ir/C (0.85 V), D-FeCo@NHC (0.85 V), and Fe_xN-NC (0.87 V) [Figure 4B]^[30-33]. As shown in Figure 4C, the Co-N₄-C, Pt/C, and NC catalysts exhibit the Tafel slopes of 103, 87, and 143 mV·dec⁻¹, respectively. In contrast, the Co-N₄Cl-C catalyst demonstrates the smallest Tafel slope (76 mV·dec⁻¹), pointing to faster oxygen electrocatalytic reaction kinetics. The TOF and mass activity of Co-N₄Cl-C and Co-N₄-C were calculated at 0.80 V vs. RHE, which serve as key indicators of intrinsic catalytic activity [Figure 4D]. The Co-N₄Cl-C catalyst exhibits a mass activity of 1,713 A·g⁻¹ and a TOF of 15.72 h⁻¹, both of which are approximately 2.5-fold greater than those of Co-N₄-C (680 A·g⁻¹ and 6.24 h⁻¹). The ORR electron transfer number for Co-N₄Cl-C was ascertained from the polarization curves obtained through the RDE measurement at rotation rates spanning 400 to 2,500 rpm within a potential window from 0.2 to 1.2 V. In accordance with the Koutecky-Levich (K-L) function in the diffusion-controlled region^[34], the Co-N₄Cl-C catalyst demonstrates a high selectivity for the four-electron transfer

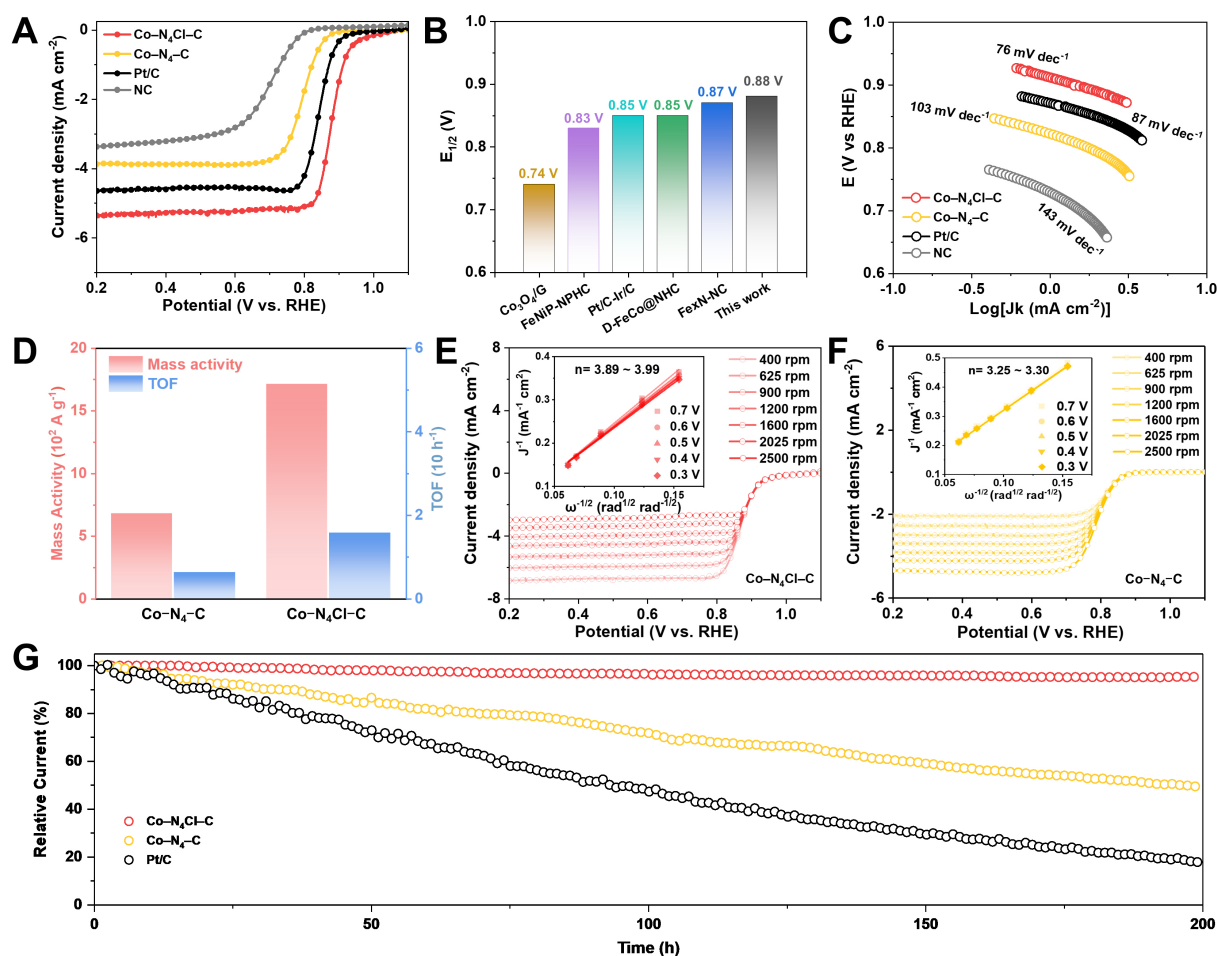


Figure 4. (A) LSV tests of Co-N₄-C, Co-N₄Cl-C, Pt/C, and NC collected after the electrolyte is saturated with O₂; (B) Literature comparison chart about ORR performance of Co-N₄Cl-C with reported catalysts; (C) Tafel plots of Co-N₄-C, Co-N₄Cl-C, Pt/C, NC; (D) Mass activity and TOF at 0.80 V (vs. RHE) for Co-N₄-C and Co-N₄Cl-C catalysts. ORR polarization curves of (E) Co-N₄Cl-C and (F) Co-N₄-C at various rotational speeds; the inset shows a fitting illustration of the K-L formula across various voltages; (G) Current-time chronoamperometric responses of Co-N₄Cl-C, Co-N₄-C, and Pt/C. LSV: Linear sweep voltammetry; ORR: oxygen reduction reaction; TOF: turnover frequency.

pathway, with an electron transfer number (n) of 3.94 [Figure 4E]. On the contrary, the electron transfer number (n) of the Co-N₄Cl-C catalyst is only 3.28 [Figure 4F]. The enhanced ORR kinetics may be attributed to the Co-N₄Cl coordination structure with broken symmetry, which experiences a more rapid reduction in the filling count of Co 3d electrons, partially evolving into the coordination-reduced Co-N₄Cl structure. This implies that there are more d -band vacant orbitals of Co single atoms available for conjugation with O 2p orbitals, hereby facilitating the adsorption of oxygen-containing species and ensuring the expeditious cleavage of the O-O bond in the *OOH intermediate on the Co single-atom sites. The rapid conversion of *OOH intermediate reduces the ORR energy barrier, which facilitates the four-electron transfer process and ensures outstanding activity in Co-N₄Cl-C^[22,50,51]. Moreover, chronoamperometric measurements were executed to quantify the long-term ORR durability of the catalysts [Figure 4G]. The Co-N₄Cl-C catalyst achieves the current density of 5.2 mA·cm⁻² at 0.3 V vs. RHE, exhibiting an excellent current retention of 96% with a decline of only 0.2 mA·cm⁻² after 200 h. This current retention rate stands in sharp contrast to 55% for Co-N₄-C and 20% for Pt/C. The significant boost in ORR performance is credited to the axial coordination of Cl atoms, which results in the formation of a localized negative charge environment

on the surface of the Co single-atom sites and suppresses the adsorption of Cl⁻ ions from the Cl-rich electrolyte^[29]. Therefore, the adsorption poisoning effect of Cl⁻ ions on the Co single-atom sites is alleviated.

The remarkable ORR activity of Co-N₄Cl-C highlights its potential as a high-performance cathode for SWZABs. The SWZAB was assembled using the Co-N₄Cl-C-based membrane electrode as the cathode and a zinc plate as the anode. Its practical charge/discharge characteristics were appraised in a simulated alkaline seawater electrolyte of 0.5 M NaCl and 6 M KOH. The open-circuit voltage (OCV) is determined to be 1.46 V, superior to that of SWZABs driven by Co-N₄-C (1.36 V) and Pt/C (1.37 V) [Figure 5A and Supplementary Figure 8]. The SWZAB employing the Co-N₄Cl-C catalyst reaches a peak power density of 179 mV·cm⁻², surpassing that of batteries manufactured using Co-N₄-C and Pt/C catalysts by 1.82-fold (98 mV·cm⁻²) and 1.25-fold (143 mV·cm⁻²), respectively [Figure 5B]. The Co-N₄Cl-C-based SWZAB reaches a specific capacity of 778 mA·h·g⁻¹ and a discharge voltage plateau of 1.27 V at a current density of 10 mA·cm⁻². In comparison, the SWZABs featuring the Co-N₄-C and Pt/C catalysts show specific capacities of only 726 and 705 mA·h·g⁻¹, respectively [Figure 5C]. In galvanostatic discharge tests [Figure 5D], the SWZAB utilizing the Co-N₄Cl-C catalyst demonstrates discharge voltage plateaus of 1.31, 1.27, and 1.25 V at current densities of 3, 5, and 10 mA·cm⁻², respectively. Upon elevating the current density from an initial value of 3 mA·cm⁻² by approximately 6.7-fold to 20 mA·cm⁻², it remains a discharge plateau of 1.21 V, achieving a retention rate of 92.3%. Notably, during periodic variations in current density, the Co-N₄Cl-C-based SWZAB maintains a distinct discharge voltage. In contrast, SWZABs incorporating Co-N₄-C and Pt/C catalysts exhibit lower voltage plateaus across diverse current densities. Meanwhile, SWZABs equipped with Co-N₄-C and Pt/C catalysts display a rapid decay in discharge voltage after 4 and 3 periods of current variation, respectively. This is attributed to their sluggish ORR kinetics, which results in a higher energy barrier, hinders the efficient transfer of electrons during the ORR process, and thereby leads to high electrochemical polarization. Moreover, a stability assessment was operationalized at a current density of 10 mA·cm⁻² [Supplementary Figure 9]. The Co-N₄Cl-C-based SWZAB exhibits remarkable stability, with a voltage gap of 1.5 V after 30 h. In stark contrast, the Co-N₄-C- and Pt/C-based SWZABs demonstrate a charge-discharge voltage differential that exceeds 2.1 V. These findings underscore the superior rate capability and reversibility of Co-N₄Cl-C under Cl-rich conditions.

CONCLUSIONS

In summary, we incorporated Cl atoms into the Co-N₄ coordination structure, developing the Co-N₄Cl-C catalyst as a high-performance ORR cathode for SWZABs. The Cl atom acts as an electron-rich and highly electronegative anionic ligand, which forms an axial coordination structure of Co-N₄Cl with Co single-atom sites in the neighboring 2D carbon layer. This axial coordination drags the original planar centrosymmetric Co-N₄ structure and stretches the bond length of Co-N, transferring electrons to the Co metal site and adjusting its charge state from +1.83 to +0.67 due to the accumulation of local negative charges caused by tip effect. The reduction in charge density boosts electronic orbital overlap between Co single-atom sites and oxygen species, thereby accelerating ORR kinetics during the conversion of *OOH intermediates. Meanwhile, the axial coordination of Cl atoms induces a localized negative charge environment on the surface of Co single atom sites, impeding the adsorption poisoning of Cl atoms. These alternations result in high intrinsic activity and stability of Co-N₄Cl-C in the alkaline seawater medium. The Co-N₄Cl-C catalyst exhibits $E_{1/2}$ of 0.88 V (vs. RHE), surpassing the values of Co₃O₄/G (0.74 V), FeNiP-NPHC (0.83 V), Pt/C-Ir/C (0.85 V), D-FeCo@NHC (0.85 V), and Fe_xN-NC (0.87 V). The SWZAB coupled with the Zn anode achieves an excellent peak power density of 179 mV·cm⁻², retaining a discharge voltage platform of 1.27 V even at 10 mA·cm⁻². This work provides new guidance for boosting the catalytic activity and durability of M-N-C catalysts in ORR applications.

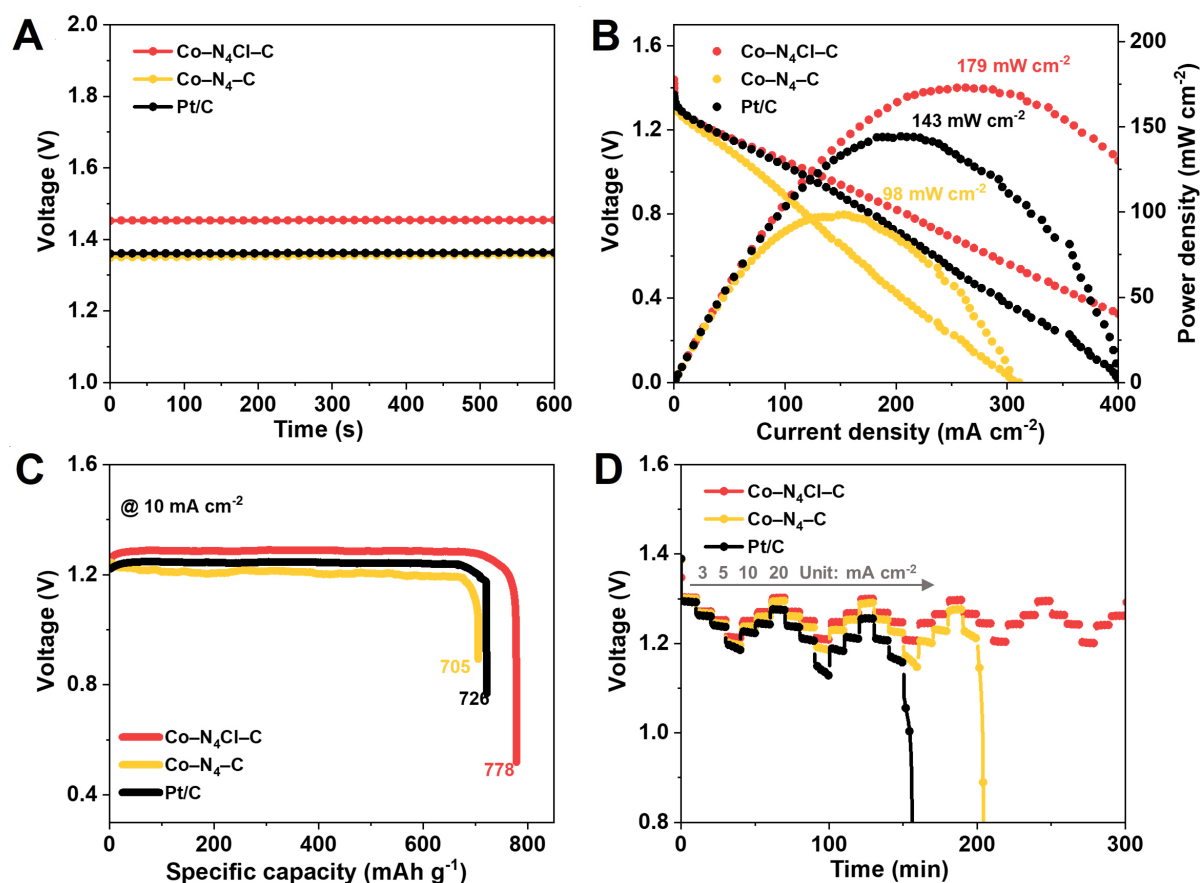


Figure 5. (A) OCV plots of SWZABs assembled with Co-N₄Cl-C, Co-N₄-C, and Pt/C catalysts using simulated alkaline seawater electrolyte (6 M KOH and 0.5 M NaCl); (B) Discharge polarization curves and power density plots of Co-N₄Cl-C-, Co-N₄-C-, and Pt/C-based SWZABs; (C) Specific capacity by mass normalization at a constant current density of 10 mA·cm⁻²; (D) Galvanostatic discharge curves at various current densities ranging from 3 to 20 cm⁻². OCV: Open-circuit voltage; SWZABs: seawater-based zinc-air batteries.

DECLARATIONS

Authors' contributions

The conception and design of the work: Zheng, X.R.; Deng, Y.D.

The acquisition and analysis of data: Jiang, X.R.; Lu, J.D.; Xie, G.D.; Li, J.H.

The interpretation of data: Jiang, X.R.; Dong, Y.; Xie, P.; Ma, W.D.

The supervision: Huang, W.J.; Zheng, X.R.; Lu, J.D.

All authors participated in writing the manuscript.

Availability of data and materials

The data and materials can be obtained from the corresponding author upon reasonable request.

Financial support and sponsorship

This work was supported by the National Natural Science Foundation of China (No. U23A20687, No. 52422314, No. 52402357) and the Hainan Provincial Natural Science Foundation of China (No. KJRC2023L04).

Conflicts of interest

Yida Deng is an Editorial Board member of the journal *Microstructures*. Yida Deng was not involved in any steps of editorial processing, notably including reviewer selection, manuscript handling, and decision making. The other authors declared that there are no conflicts of interest.

Ethical approval and consent to participate

Not applicable.

Copyright

© The Author(s) 2025.

REFERENCES

1. Yu, J.; Li, B. Q.; Zhao, C. X.; Zhang, Q. Seawater electrolyte-based metal-air batteries: from strategies to applications. *Energy. Environ. Sci.* **2020**, *13*, 3253-68. [DOI](#)
2. Wang, Q.; Kaushik, S.; Xiao, X.; Xu, Q. Sustainable zinc-air battery chemistry: advances, challenges and prospects. *Chem. Soc. Rev.* **2023**, *52*, 6139-90. [DOI](#) [PubMed](#)
3. Guo, Y.; Cao, Y.; Lu, J.; Zheng, X.; Deng, Y. The concept, structure, and progress of seawater metal-air batteries. *Microstructures* **2023**, *3*, 2023038. [DOI](#)
4. Zheng, L.; Chang, L.; Xue, S.; et al. Electrochemical responsive alginate chains rendered sol-to-gel gradient electrolyte towards practical Ah-level zinc metal pouch cell. *Angew. Chem. Int. Ed. Engl.* **2025**, *64*, e202502103. [DOI](#) [PubMed](#)
5. Ju, L.; Tang, X.; Kou, L. Polarization boosted catalysis: progress and outlook. *Microstructures* **2022**, *2*, 2022008. [DOI](#)
6. Dey, S.; Mondal, B.; Chatterjee, S.; Rana, A.; Amanullah, S. K.; Dey, A. Molecular electrocatalysts for the oxygen reduction reaction. *Nat. Rev. Chem.* **2017**, *1*, 0098. [DOI](#)
7. Zhan, Y.; Ding, Z. B.; He, F.; et al. Active site switching of Fe-N-C as a chloride-poisoning resistant catalyst for efficient oxygen reduction in seawater-based electrolyte. *Chem. Eng. J.* **2022**, *443*, 136456. [DOI](#)
8. Zhang, J.; Yuan, Y.; Gao, L.; Zeng, G.; Li, M.; Huang, H. Stabilizing Pt-based electrocatalysts for oxygen reduction reaction: fundamental understanding and design strategies. *Adv. Mater.* **2021**, *33*, e2006494. [DOI](#) [PubMed](#)
9. Li, Y.; Liang, J.; Lin, Z.; et al. Introducing covalent metal-phosphorus bonds into intermetallic platinum-based catalysts for high-performance fuel cells. *Renewables* **2024**, *2*, 223-32. [DOI](#)
10. Zeng, K.; Zheng, X.; Li, C.; et al. Recent advances in non-noble bifunctional oxygen electrocatalysts toward large-scale production. *Adv. Funct. Mater.* **2020**, *30*, 2000503. [DOI](#)
11. Osgood, H.; Devaguptapu, S. V.; Xu, H.; Cho, J.; Wu, G. Transition metal (Fe, Co, Ni, and Mn) oxides for oxygen reduction and evolution bifunctional catalysts in alkaline media. *Nano. Today* **2016**, *11*, 601-25. [DOI](#)
12. Han, X.; He, G.; He, Y.; et al. Metal air batteries: engineering catalytic active sites on cobalt oxide surface for enhanced oxygen electrocatalysis. *Adv. Energy. Mater.* **2018**, *8*, 1870043. [DOI](#)
13. Pu, Z.; Liu, T.; Amiin, I. S.; et al. Transition-metal phosphides: activity origin, energy-related electrocatalysis applications, and synthetic strategies. *Adv. Funct. Materials* **2020**, *30*, 2004009. [DOI](#)
14. Tian, D.; Denny, S. R.; Li, K.; Wang, H.; Kattel, S.; Chen, J. G. Density functional theory studies of transition metal carbides and nitrides as electrocatalysts. *Chem. Soc. Rev.* **2021**, *50*, 12338-76. [DOI](#) [PubMed](#)
15. Maiti, S.; Maiti, K.; Curnan, M. T.; Kim, K.; Noh, K.; Han, J. W. Engineering electrocatalyst nanosurfaces to enrich the activity by inducing lattice strain. *Energy. Environ. Sci.* **2021**, *14*, 3717-56. [DOI](#)
16. Hu, X.; Tian, W.; Wu, Z.; Li, X.; Li, Y.; Wang, H. Synthesis of Zr₂ON₂ via a urea-glass route to modulate the bifunctional catalytic activity of NiFe layered double hydroxide in a rechargeable zinc-air battery. *J. Colloid. Interface. Sci.* **2024**, *672*, 610-7. [DOI](#) [PubMed](#)
17. Poudel, M. B.; Balanay, M. P.; Lohani, P. C.; Sekar, K.; Yoo, D. J. Atomic engineering of 3D self-supported bifunctional oxygen electrodes for rechargeable zinc-air batteries and fuel cell applications. *Adv. Energy. Mater.* **2024**, *14*, 2400347. [DOI](#)
18. He, Y.; Liu, S.; Priest, C.; Shi, Q.; Wu, G. Atomically dispersed metal-nitrogen-carbon catalysts for fuel cells: advances in catalyst design, electrode performance, and durability improvement. *Chem. Soc. Rev.* **2020**, *49*, 3484-524. [DOI](#) [PubMed](#)
19. Yuan, L. J.; Sui, X. L.; Pan, H.; Wang, Z. B. Strategies and mechanism for enhancing intrinsic activity of metal-nitrogen-carbon catalysts in electrocatalytic reactions. *Renewables* **2023**, *1*, 514-40. [DOI](#)
20. Shang, H.; Zhou, X. L.; Dong, J.; Wang, Z. Engineering unsymmetrically coordinated Cu-S₁N₃ single atom sites with enhanced oxygen reduction activity. *Nat. Commun.* **2020**, *11*, 3049. [DOI](#) [PubMed](#) [PMC](#)
21. Mun, Y.; Lee, S.; Kim, K.; et al. Versatile strategy for tuning ORR activity of a single Fe-N₄ site by controlling electron-withdrawing/donating properties of a carbon plane. *J. Am. Chem. Soc.* **2019**, *141*, 6254-62. [DOI](#) [PubMed](#)
22. Liu, M.; Zhang, J.; Su, H.; et al. *In situ* modulating coordination fields of single-atom cobalt catalyst for enhanced oxygen reduction reaction. *Nat. Commun.* **2024**, *15*, 1675. [DOI](#) [PubMed](#) [PMC](#)

23. Grimaud, A.; Demortière, A.; Saubanère, M.; et al. Activation of surface oxygen sites on an iridium-based model catalyst for the oxygen evolution reaction. *Nat. Energy*. **2016**, *2*, 1-10. DOI
24. Wang, A.; Li, J.; Zhang, T. Heterogeneous single-atom catalysis. *Nat. Rev. Chem.* **2018**, *2*, 65-81. DOI
25. Zhou, A. W.; Wang, D. S.; Li, Y. D. Hollow microstructural regulation of single-atom catalysts for optimized electrocatalytic performance. *Microstructures* **2022**, *2*, 2022005. DOI
26. Wang, Z.; Niu, H.; Wu, T.; Ding, S.; Yu, X. B.; Su, Y. Periodic defect boundary-mediated activity of electrocatalytic oxygen reduction reactions of Fe-N-C catalysts. *Renewables* **2024**, *3*, 213-9. DOI
27. Wang, W.; Hu, Y.; Li, P.; Liu, Y.; Chen, S. Realizing the $4e^-/2e^-$ pathway transition of O_2 reduction on Co-N₄-C catalysts by regulating the chemical structures beyond the second coordination shells. *ACS. Catal.* **2024**, *14*, 5961-71. DOI
28. Datye, A. K.; Guo, H. Single atom catalysis poised to transition from an academic curiosity to an industrially relevant technology. *Nat. Commun.* **2021**, *12*, 895. DOI PubMed PMC
29. Liu, Y.; Feng, S.; Shan, L.; et al. Localized negatively charged interfaces for seawater electrolyte-based zinc-air batteries. *Adv. Funct. Materials*. **2025**, *35*, 2422874. DOI
30. Yu, J.; Zhao, C. X.; Liu, J. N.; Li, B. Q.; Tang, C.; Zhang, Q. Seawater-based electrolyte for zinc-air batteries. *GreenChE* **2020**, *1*, 117-23. DOI
31. Yu, Q.; Liu, X.; Liu, G.; et al. Constructing three-phase heterojunction with 1D/3D hierarchical structure as efficient trifunctional electrocatalyst in alkaline seawater. *Adv. Funct. Materials*. **2022**, *32*, 2205767. DOI
32. Wu, S.; Liu, X.; Mao, H.; et al. Realizing high-efficient oxygen reduction reaction in alkaline seawater by tailoring defect-rich hierarchical heterogeneous assemblies. *Appl. Catal. B-Environ.* **2023**, *330*, 122634. DOI
33. Wu, S.; Liu, X.; Mao, H.; et al. Unraveling the tandem effect of nitrogen configuration promoting oxygen reduction reaction in alkaline seawater. *Adv. Energy. Mater.* **2024**, *14*, 2400183. DOI
34. Luo, Y.; Li, K.; Hu, Y.; et al. TiN as radical scavenger in Fe-N-C aerogel oxygen reduction catalyst for durable fuel cell. *Small* **2024**, *20*, e2309822. DOI PubMed
35. Meng, R.; Zhang, C.; Lu, Z.; et al. An oxygenophilic atomic dispersed Fe-N-C catalyst for lean-oxygen seawater batteries. *Adv. Energy. Mater.* **2021**, *11*, 2170085. DOI
36. Zhang, J.; Liu, M.; Zhang, Y.; et al. Tandem synergetic effect in symbiotic Co catalyst for enhanced oxygen reduction. *Chem. Eng. J.* **2025**, *505*, 159687. DOI
37. Zhang, W.; Zhang, J.; Wang, N.; et al. Two-electron redox chemistry via single-atom catalyst for reversible zinc-air batteries. *Nat. Sustain.* **2024**, *7*, 463-73. DOI
38. Wang, K.; Lu, Z.; Lei, J.; Liu, Z.; Li, Y.; Cao, Y. Modulation of ligand fields in a single-atom site by the molten salt strategy for enhanced oxygen bifunctional activity for zinc-air batteries. *ACS. Nano.* **2022**, *16*, 11944-56. DOI
39. Feng, X.; Chen, G.; Cui, Z.; et al. Engineering electronic structure of nitrogen-carbon sites by sp^3 -hybridized carbon and incorporating chlorine to boost oxygen reduction activity. *Angew. Chem. Int. Ed. Engl.* **2024**, *63*, e202316314. DOI PubMed
40. Tian, H.; Ma, Y.; Li, Z.; et al. Disorder-tuned conductivity in amorphous monolayer carbon. *Nature* **2023**, *615*, 56-61. DOI PubMed
41. Cui, J.; Zhang, D.; Liu, Z.; et al. Carbon-anchoring synthesis of Pt₁Ni₁@Pt/C core-shell catalysts for stable oxygen reduction reaction. *Nat. Commun.* **2024**, *15*, 9458. DOI PubMed PMC
42. Zhang, H.; Guo, H.; Li, D.; et al. Halogen doped graphene quantum dots modulate TDP-43 phase separation and aggregation in the nucleus. *Nat. Commun.* **2024**, *15*, 2980. DOI PubMed PMC
43. Huang, Y.; Zhu, K.; Hu, Z.; et al. Solvent-free synthesis of foam board-like CoSe₂ alloy to selectively generate singlet oxygen via peroxymonosulfate activation for sulfadiazine degradation. *J. Hazard. Mater.* **2024**, *466*, 133611. DOI PubMed
44. Su, J.; Musgrave, C. B.; Song, Y.; et al. Strain enhances the activity of molecular electrocatalysts via carbon nanotube supports. *Nat. Catal.* **2023**, *6*, 818-28. DOI
45. Kumar, P.; Kannimuthu, K.; Zeraati, A. S.; et al. High-density cobalt single-atom catalysts for enhanced oxygen evolution reaction. *J. Am. Chem. Soc.* **2023**, *145*, 8052-63. DOI PubMed
46. Ye, P.; Fang, K.; Wang, H.; et al. Lattice oxygen activation and local electric field enhancement by co-doping Fe and F in CoO nanoneedle arrays for industrial electrocatalytic water oxidation. *Nat. Commun.* **2024**, *15*, 1012. DOI PubMed PMC
47. Ding, S.; Barr, J. A.; Shi, Q.; et al. Engineering atomic single metal-FeN₄Cl sites with enhanced oxygen-reduction activity for high-performance proton exchange membrane fuel cells. *ACS. Nano.* **2022**, *16*, 15165-74. DOI PubMed
48. Liu, P.; Chen, B.; Liang, C.; et al. Tip-enhanced electric field: a new mechanism promoting mass transfer in oxygen evolution reactions. *Adv. Mater.* **2021**, *33*, e2007377. DOI PubMed
49. Khan, M. U.; Wang, L.; Liu, Z.; et al. Pt₃Co octapods as superior catalysts of CO₂ hydrogenation. *Angew. Chem. Int. Ed. Engl.* **2016**, *55*, 9548-52. DOI PubMed
50. Zhang, L.; Jin, N.; Yang, Y.; et al. Advances on axial coordination design of single-atom catalysts for energy electrocatalysis: a review. *Nanomicro. Lett.* **2023**, *15*, 228. DOI PubMed PMC
51. Sabhapathy, P.; Raghunath, P.; Sabbah, A.; et al. Axial chlorine induced electron delocalization in atomically dispersed FeN₄ electrocatalyst for oxygen reduction reaction with improved hydrogen peroxide tolerance. *Small* **2023**, *19*, e2303598. DOI PubMed